ACS NANO

www.acsnano.org

ARTICLE

Colloidal Clusters and Networks Formed by Oppositely Charged Nanoparticles with Varying Stiffnesses

Sofia M. Morozova, Leticia López-Flores, Albert Gevorkian, Honghu Zhang, Vahid Adibnia, Weiqing Shi, Dmytro Nykypanchuk, Tatiana G. Statsenko, Gilbert C. Walker, Oleg Gang, Monica Olvera de la Cruz,* and Eugenia Kumacheva*

Cite This: *ACS Nano* 2023, 17, 15012−15024

Read Online

ACCESS | Metrics & More | Article Recommendations | Supporting Information

ABSTRACT: **Colloidal clusters and gels are ubiquitous in science and technology. Particle softness has a strong effect on interparticle interactions; however, our understanding of the role of this factor in the formation of colloidal clusters and gels is only beginning to evolve. Here, we report the results of experimental and simulation studies of the impact of particle softness on the assembly of clusters and networks from mixtures of oppositely charged polymer nanoparticles (NPs). Experiments were performed below or above the polymer glass transition temperature, at which the interaction potential and adhesive forces between the NPs were significantly varied. Hard NPs assembled in fractal clusters that subsequently organized in a kinetically arrested colloidal gel, while soft NPs formed dense precipitating aggregates, due to the NP deformation and the decreased interparticle distance. Importantly, interactions of hard and soft NPs led to the formation of discrete precipitating NP aggregates at a relatively low volume fraction of soft NPs. A phenomenological model was developed for interactions of oppositely charged NPs with varying softnesses. The experimental results were in agreement with molecular dynamics simulations based on the model. This work provides insight on interparticle interactions before, during, and after the formation of hard−hard, hard−soft, and soft−soft contacts and has impact for numerous applications of reversible colloidal gels, including their use as inks for additive manufacturing.**

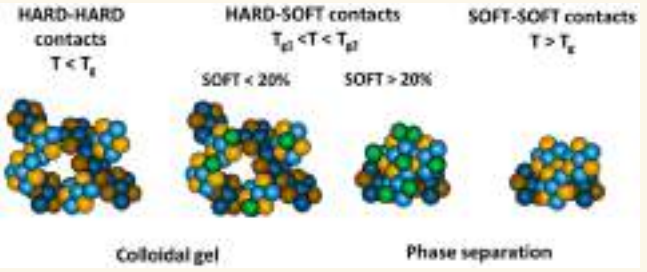

KEYWORDS: *colloidal gel, nanoparticles, fractal clusters, soft potential, diffusion-limited cluster aggregation, phase separation*

INTRODUCTION

Colloidal clusters and gels form when interparticle attraction dominates over the particle repulsive interactions and thermal energy. Particle bonding is achieved via chemical mechanisms or physical interactions such as van der Waals,[1] solvation,[2] hydrophobic,[3] electrostatic,[4] and steric[5] forces. Even at low particle volume fractions, assembly of colloidal clusters and gels drastically changes the properties of complex fluids and thus has implications for their use in science and technology, e.g., in the food industry,[6] personal care products,[7,8] and biotechnologies.[9−11] In particular, physically cross-linked colloidal gels have promising applications as inks in additive manufacturing, e.g., extrusion-based 3D printing.[12,13] Owing to the disruption of physical bonds with an increasing shear rate, such gels exhibit reduction in viscosity with an increasing shear rate (that is, shear thinning), which enables smooth flow of an ink through a nozzle under relatively low applied pressures. On the other hand, fundamentally, studies of the behavior of colloidal clusters and gels contribute to our understanding of out-of-equilibrium systems.

The established mechanisms of colloidal gel formation include diffusion-limited cluster aggregation (DLCA),[14,15] reaction-limited cluster aggregation (RLCA),[16,17] and kinetic arrest following spinodal decomposition.[18−20] The state of the system is generally described by a phase diagram plotted in the coordinates of particle volume fraction−thermal energy, k_BT. The diagram includes the regions of a stable particle dispersion (a gas state), a gel, a glass, a colloidal crystal, and a phase-separated system with a coagulated precipitate.[14,21−24]

Received: May 6, 2023
Accepted: July 10, 2023
Published: July 17, 2023

https://doi.org/10.1021/acsnano.3c04064
ACS Nano 2023, 17, 15012−15024

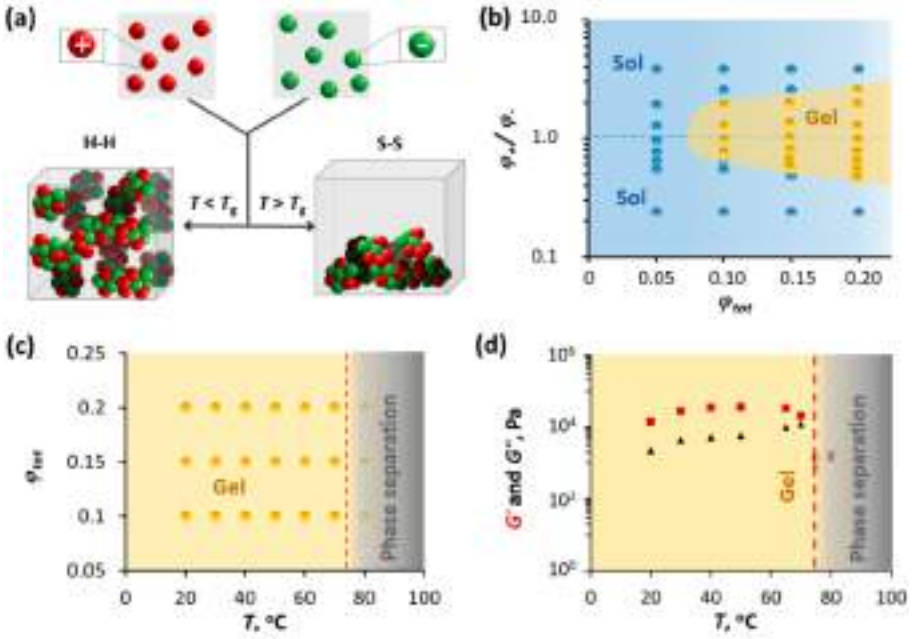

Figure 1. Temperature-dependent state of the colloidal mixture. (a) Schematic of mixing of oppositely charged NPs at the temperature below (left) and above (right) T_g, leading to H-H and S-S interparticle contacts, respectively. (b) State diagram for the mixture of 400 nm diameter p(EtMA)$^+$/p(EtMA)$^-$ NPs at 22 °C. (c) Temperature-dependent state diagram of the NP mixture as in (b) at $\varphi+/\varphi-$ = 1.0. (d) Variation in the storage modulus (G', red square symbols) and loss modulus (G'', black triangle symbols) of the mixture of 400 nm p(EtMA)$^+$/p(EtMA)$^-$ NPs at $\varphi+/\varphi-$ = 1.0 and φ_{tot} = 0.15. In (c) and (d), the vertical dashed lines correspond to T_g of the polymer.

Most experimental and theoretical studies have focused on clusters and networks formed by particles interacting via depletion forces[25,26] or mixtures of oppositely charged colloids.[19,27,28] In both cases, upon collision, the particles were assumed to form an elastic Hertzian contact;[14,18,29] however, particle stiffness may be an important factor influencing interactions between colloids.[30−33] For adhesive soft particles, the contact area (the Johnson−Kendall−Roberts contact) is larger than for hard colloids and, upon separation, such particles exhibit enhanced adhesion, compared to their hard counterparts.[1] A special case of soft particles are micelles[34] and microgels.[31,32,35] When brought in contact, these branched particles exhibit partial interpenetration and solvent expulsion.[36,37] The mechanisms of the formation of colloidal clusters and networks from mixtures of condensed colloids with varying stiffnesses are not well-established.

Here we report the results of experimental and simulation studies of colloidal clusters and networks formed by oppositely charged condensed polymer nanoparticles (NPs) with different stiffnesses. In the mixture, the same-charge NPs exhibited repulsion, while oppositely charged NPs attracted each other. For the NPs with close-to-equal dimensions and symmetrical opposite charges, the effect of hard−hard, hard−soft, or soft−soft interparticle contacts was explored by conducting experiments below and above the polymer glass transition temperature, T_g, at which strong adhesion existed for the hard−soft and soft−soft NP contacts. Below T_g, a reversible colloidal network (a gel) formed from fractal-type clusters of rigid NPs. Above T_g, the NPs formed compact aggregates that exhibited synergy and rapidly precipitated. Surprisingly, the addition of a small fraction of soft NPs to a mixture of oppositely charged hard NPs triggered the formation of discrete NP aggregates. We developed a phenomenological model and conducted simulations to explore interactions of oppositely charged NPs with varying softnesses. The results of simulations revealed the decrease in the interparticle distance for soft−soft and soft−hard interparticle contacts, in comparison with hard−hard contacts, which resulted in the formation of densified precipitating nanostructures. The results of this work shed light on the role of particle stiffness on interparticle interactions and their role in the formation of colloidal clusters and networks.

RESULTS

Colloidal Interactions with the Formation of Hard−Hard or Soft−Soft Interparticle Contacts. We studied the formation of colloidal clusters and gels from mixtures of positively and negatively charged polymer NPs that had close-to-equal average diameters and absolute values of electrokinetic potentials (ζ potentials). Experiments were carried out by mixing dispersions of oppositely charged 60, 150, or 400 nm diameter NPs at a temperature below or above the polymer glass transition temperature, T_g, and examining the state and properties of the resulting colloidal mixture by imaging, rheology, small angle X-ray Scattering (SAXS), and static light scattering (SLS). We refer to the particles mixed at the temperature $T < T_g$ as "hard" NPs forming hard−hard (H-H) contacts, and the particles mixed at $T > T_g$ as "soft" NPs forming soft−soft (S-S) contacts and undergoing deformation in interparticle contacts, as defined in the theoretical model. Mixing dispersions of oppositely charged NPs was carried out by heating each NP dispersion to a particular temperature and subsequently dropwise adding one dispersion to another one. The total volume fraction, φ_{tot}, of the NPs in the mixture was in the range 0.05−0.20, and the volume fractions of cationic and anionic NPs were denoted as $\varphi+$ and $\varphi-$, respectively.

Experiments were conducted with positively and negatively charged poly(ethyl methacrylate) latex NPs (p(EtMA)$^+$ and

https://doi.org/10.1021/acsnano.3c04064
ACS Nano 2023, 17, 15012−15024

p(EtMA)$^-$ NPs, respectively) with average diameters D_h of 60 ± 5, 150 ± 12, and 400 ± 20 nm. The corresponding absolute values of ζ potential were |57 ± 7|, |51 ± 6|, and |40 ± 3| mV. In each mixture, oppositely charged NPs had a size ratio of 1.01. The details of NP synthesis and properties are provided in Table S1 and Figure S1 in the Supporting Information, respectively. The T_g of the NPs was 75 °C (Table S2, Supporting Information). Dispersions of same-charge NPs were colloidally stable over the entire temperature range in this study, and NP dimensions and ζ potentials did not notably change over the temperature interval from 25 to 65 °C (Figure S2, Supporting Information).

Two distinct states of the colloidal mixture were observed when individual NP dispersions were mixed at temperatures below and above T_g. At φ_{tot} exceeding a threshold value, a space-filling kinetically arrested colloidal gel formed at $T < T_g$ (Figure 1a, left). At $T > T_g$, the NP mixture separated into the NP-deprived liquid phase and compacted, rapidly precipitating colloidal aggregates (Figure 1a, right).

We first examined the effect of φ_{tot} and the $\varphi+/\varphi-$ ratio of oppositely charged NPs on the state of the colloidal mixture. Figure 1b shows the system state diagram, plotted in the coordinates of the φ_{tot} and $\varphi+/\varphi-$ ratio. Upon mixing the NP dispersions, for $\varphi_{tot} < 0.10$ and at $0.1 < \varphi+/\varphi- < 10$, the mixture remained in the sol ("gas") state, shown as a blue region in Figure 1b, although the formation of small discrete clusters of oppositely charged NPs was possible. At $\varphi_{tot} \geq 0.10$, the state of the system depended on the ratio $\varphi+/\varphi-$. A colloidal gel formed in the close-to-symmetrical region highlighted with a yellow color (Figure 1b). With an increasing φ_{tot}, the gel region broadened with respect to the $\varphi+/\varphi-$ ratio due to the accommodated deviation from the stoichiometry of oppositely charged NPs. The gel was reversible with respect to dilution or application of a shear strain (Figure S3, Supporting Information). Mixtures of oppositely charged NPs with D_h values of 60 and 150 nm exhibited temperature-dependent gelation similar to that of the NPs with a D_h value of 400 nm (Figure S4, Supporting Information).

Next, for $\varphi+/\varphi- = 1.0$ and φ_{tot} values of 0.10, 0.15, and 0.2 (corresponding to the gel region in Figure 1b), the state of the system was examined in the temperature range $20 \leq T \leq 80$ °C (Figure 1c). At $20 \leq T \leq 70$ °C, the NP mixture formed a gel, while at $T \geq 75$ °C (the T_g of the polymer), the formation of dense rapidly settling NP aggregates took place, which were not redispersed upon cooling, sonication, or the application of shear. Nanoparticle volume fraction in the aggregates was 0.35, compared with $\varphi_{tot} = 0.15$ for the corresponding original NP mixture dispersion.

Figure 1d shows the temperature-dependent variation of the rheological properties of the NP mixture. At $20 \leq T < 75$ °C, the relationship $G' > G''$ and $\tan\delta < 1$ corresponded to the gel state, where G' and G'' are the storage and loss shear modulus of the gel, respectively, and $\tan\delta$ ($=G''/G'$) is a measure of the elasticity of the gel ($\tan\delta < 1$). A weak increase of G' and G'' was observed with the temperature increase from 20 to 65 °C, due to the formation of stronger NP contacts. A gradual reduction in G' and G'' values started at 70 °C, with $\tan\delta$ increasing from 0.3 to 0.6, and at $T = 75$ °C, both G' and G'' drastically decreased. At 80 °C, massive NP aggregation took place. A temperature ramp experiment conducted at a heating rate of 1 °C/min in the temperature range from 20 to 80 °C led to similar results (Figure S3, Supporting Information).

The temperature-dependent behavior of the colloidal mixture was further examined by imaging clusters of oppositely charged hard or soft 400 nm diameter NPs. Anionic and cationic NPs were labeled with a fluorescein acrylate dye (λ_{ex} = 488, λ_{em} = 525) and Nile Red (λ_{ex} = 554 nm, λ_{em} = 630 nm), respectively (Figure S5, Supporting Information). We ensured that dye labeling did not change the T_g of the polymer (Table S2, Supporting Information). Dilute NP dispersions were mixed at temperatures below or above T_g. Figure 2 shows

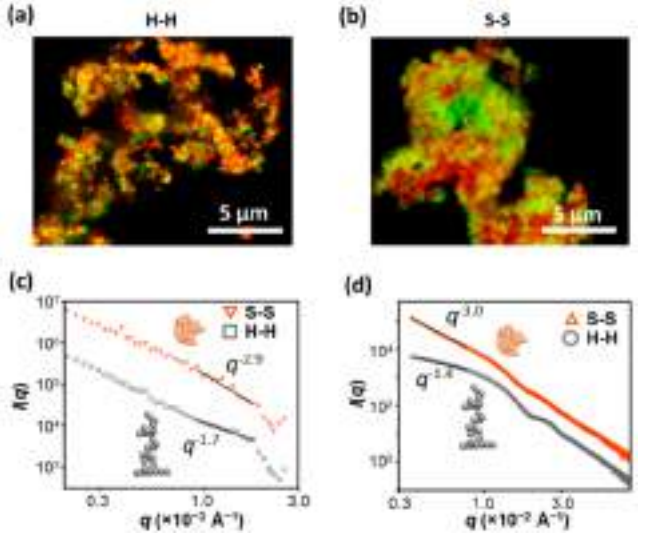

Figure 2. Temperature-dependent formation of NP clusters. (a, b) Confocal fluorescence microscopy images of clusters of 400 nm diameter p(EtMA)$^+$ and p(EtMA)$^-$ NPs formed at φ_{tot} = 0.05 and at $\varphi+/\varphi-$ = 1.0 at 22 °C (a) and 80 °C (b). The images were taken 1 min after NP mixing. (c) SLS intensity profiles for clusters of 400 nm diameter p(EtMA)$^+$and p(EtMA)$^-$ NPs formed at 22 and 80 °C, corresponding to H-H and S-S contacts, respectively. (d) SAXS intensity profiles for clusters of 60 nm diameter p(EtMA)$^+$and p(EtMA)$^-$ NPs formed at 22 and 80 °C, acquired 20 min after NP mixing. The black solid lines in (c) and (d) are power law fits to the data in the q ranges. Insets in (c) and (d) schematically illustrate the morphology of NP clusters with fractal dimensions obtained from SLS and SAXS experiments, respectively.

confocal fluorescence microscopy images of the NP clusters assembled at 22 and 80 °C (corresponding to the formation of H-H and S-S contacts, respectively). Hard NPs formed open-structure clusters with discernible individual NPs (Figure 2a), whereas soft NPs assembled into large compact spheroid-shaped aggregates with average dimensions in the range 4.0–20 μm and unresolved individual NPs (Figure 2b). In addition, hard NPs with different charges were uniformly distributed throughout the clusters, while aggregates of soft NPs had a heterogeneous structure. The fractal dimension, d_f, of the NP clusters was determined by using the box counting method for the analysis of the confocal fluorescence microscopy images.[38,39] The clusters with H-H and S-S contacts had d_f values of 1.55 ± 0.22 and 2.61 ± 0.35, which corresponded to open dendritic structures and compact aggregates, respectively.

The structure of NP clusters was further examined by SLS using 400 nm NPs (Figure 2c) and SAXS using 60 nm NPs (Figure 2d and Figure S6a, Supporting Information). The SLS covered the length scale of 250 nm to 3 μm, while in the SAXS experiments, the nanoscale regime, with lengths up to 180 nm, was examined. Both methods provided information about the

https://doi.org/10.1021/acsnano.3c04064
ACS Nano 2023, 17, 15012–15024

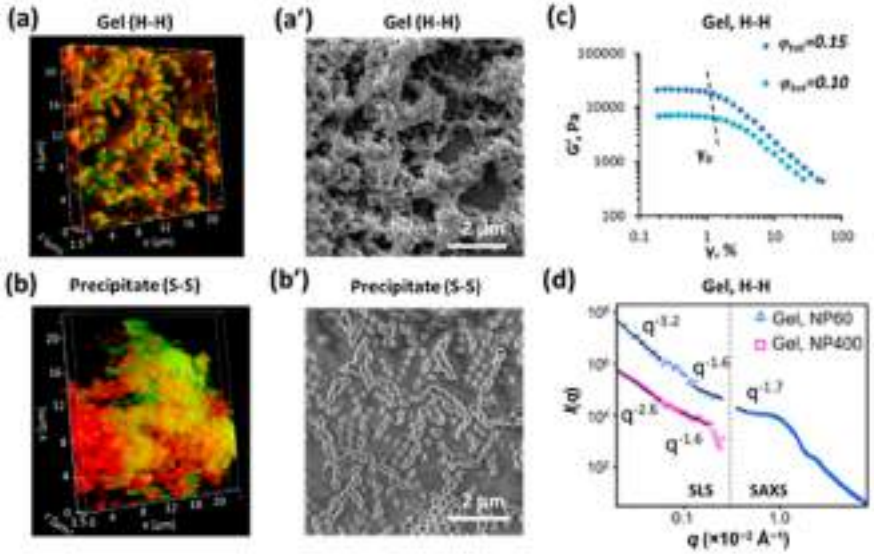

Figure 3. Structure and properties of the colloidal gel and NP aggregates. (a, a′) Confocal fluorescence microscopy (a) and SEM (a′) images of the gel formed by hard 400 nm diameter p(EtMA)$^+$and p(EtMA)$^-$ NPs at 22 °C. (b, b′) Confocal fluorescence microscopy (b) and SEM (b′) images of the NP aggregate formed at 80 °C. The image in (b′) shows cracks in the polymer film. (c) Variation in G' vs the shear strain γ, plotted at different φ_{tot} values and used to determine the fractal dimension, d_f, of the gel and aggregates. The dashed line shows the strain γ_0, at which the value of G' was reduced by 10%. (d) SLS and SAXS intensity profiles of the colloidal gels formed by 60 and 400 nm diameter p(EtMA)$^+$ and p(EtMA)$^-$ NPs. Power law fitting (black lines) was applied to the different q ranges, and the extracted slopes (as shown) were indicative of scatterers fractal dimension, d_f. In all experiments, φ_{tot} = 0.15 and $\varphi+/\varphi-$ = 1.0. In all experiments, φ_{tot} = 0.15 and $\varphi+/\varphi-$ = 1.0 were used.

structure of clusters and their NP building blocks, based on the intensities at low and high q ranges, that is, $q < 1/R$ and $q > 1/R$, respectively, where q is the scattering vector and R is the NP radius. The scattering profiles at $q < 1/R$ exhibited a power-law dependence $I(q) \propto q^{-\alpha}$, characteristic of a mass or surface fractal system (where $I(q)$ is the scattering intensity as a function of a momentum transfer q and α are a characteristic exponent and a slope in log−log $I(q)$ plots, respectively).[40−42] For a mass fractal, $1.0 \leq \alpha \leq 3.0$ and $d_f = \alpha$, while for a surface fractal, $3.0 \leq \alpha \leq 4.0$ and $d_f = 6 - \alpha$ (see details in the Supporting Information). Clusters of hard NPs (H-H contacts) exhibited d_f values of 1.7 ± 0.1 and 1.4 ± 0.1 for 400 and 60 nm diameter NPs, respectively (Figure 2c,d), while soft NPs (S-S contacts) formed clusters with d_f values of ∼3.0 (2.9 ± 0.1 and 3.0 ± 0.1 for 400 and 60 nm diameter NPs, respectively). These results show that for the same type of interparticle contacts similar fractal dimensions were obtained for the NPs with more than 6-fold size difference, which were examined by imaging and scattering methods. Furthermore, within the examined length scales, a significant difference in the value of d_f for the NP clusters formed via H-H and S-S interparticle contacts agreed with the results of the image analysis.

At $\varphi_{tot} \geq 0.10$, in less than 1 min, the clusters of hard NPs assembled in a colloidal network, as shown in the fluorescence microscopy and SEM images in Figure 3a,a′, respectively. In both cases, the network had a branched structure, with NPs retaining a spherical shape. In Figure 3a, individual cationic NPs (red) and anionic NPs (green) were clearly discerned. In contrast, the precipitated aggregates of soft NPs had a dense heterogeneous structure with almost indistinguishable individual NPs (Figure 3b). The SEM images of these aggregates revealed NP coalescence occurring over time (Figure 3b′).

The difference between the structure of the colloidal gel and precipitated NP aggregates was also examined in rheology experiments by utilizing an elasticity model for cluster-derived colloidal gels.[43] The strength of the H-H contacts in the gel was related to their disruption at strain γ_0, at which the value of G' was reduced by 10% (Figure 3c). By analyzing the variation γ_0 vs. φ_{tot} and G' vs φ_{tot}, we determined d_f = 1.87 ± 0.1 for the gel (Figure S7, Supporting Information). This d_f value was approximately 30% higher than d_f = 1.40 ± 1.0 determined by SAXS for the NP clusters; however, it has been established that fractal dimensions of clusters are smaller than those in the gel, due to a greater number of NP neighbors in the network.[44]

To examine the morphology and structure of the colloidal gels on a large length scale, SLS measurements were performed for the gels formed by 60 and 400 nm NPs, complementary to SAXS experiments for the gels assembled from 60 nm NPs (Figure 3d). The scattering intensity profiles at $q < 1/R$ from both 60 and 400 nm NP gels showed dissimilar power law slopes for different q regions, which signified that a fractal dimension of the formed gel was scale-variable.[45] More specifically, on a scale of a few NP diameters, small NP aggregates exhibited an open and branched structure, as concluded from d_f = 1.6−1.7, similar to the structures observed in the NP clusters (Figure 2c,d). Next, these small aggregates formed 3D aggregates with a larger fractal dimension. For example, at length scales of 1−3 μm (up to the lower q limit of SLS), the gels formed by 60 and 400 nm NPs showed exponent α values of 3.2 ± 0.2 and 2.6 ± 0.1, respectively, which indicated a denser 3D structure. For both NP types, an increase of fractal dimensions at larger probed scales revealed the transition from low-dimension mass fractal structures to 3D objects with surface fractals.[45] For the gels formed by 60 nm NPs, a broad scattering peak observed at $q \approx 0.01$ Å^{-1} corresponded to the interparticle distances of 60 nm NPs and

https://doi.org/10.1021/acsnano.3c04064
ACS Nano 2023, 17, 15012−15024

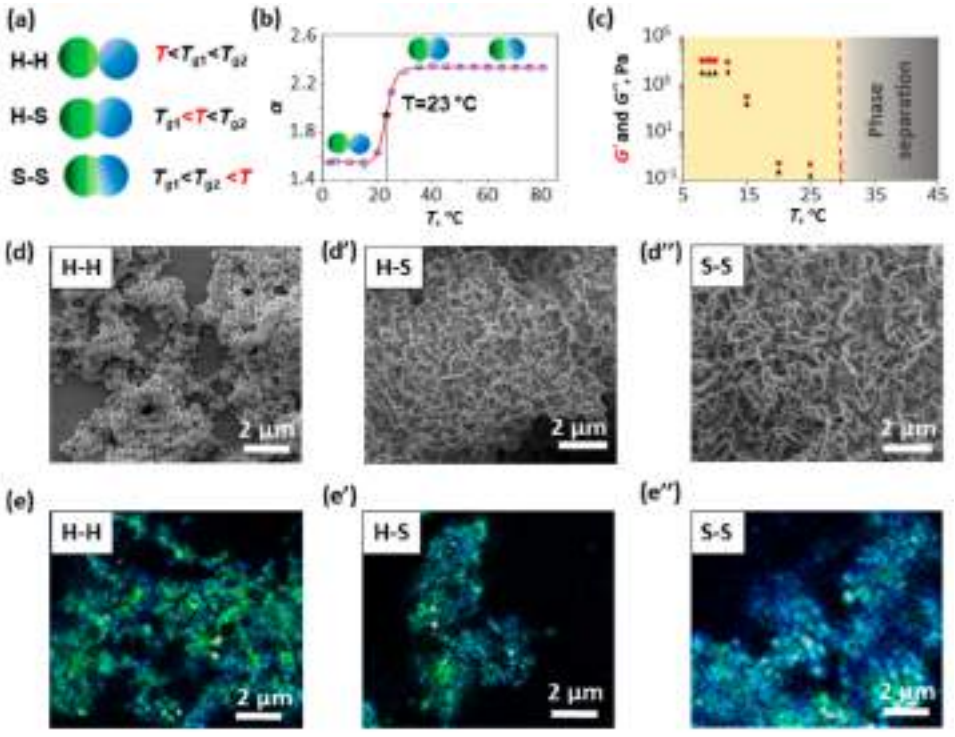

Figure 4. Interactions between oppositely charged hard and soft NPs. (a) Illustration of hard−hard (H-H), hard−soft (H-S) and soft−soft (S-S) interparticle contacts. (b) Dependence of $I(q)$ exponent α vs temperature, extracted from intensity profiles in the in situ SAXS experiment for clusters of p(VAc)$^+$ and p(EtMA)$^-$ NPs formed at 5 °C and heated to 80 °C. (c) Variation in G' (red square symbols) and G'' (black triangle symbols) with the temperature for the mixture of p(VAc)$^+$ and p(EtMA)$^-$ NPs. In (b) and (c), the NP diameter was 60 ± 6 nm. (d, d′, d″) SEM images of the p(VAc)$^+$/p(EtMA)$^-$ NP mixture at (d) 10, (d′) 22, and (d″) 80 °C. (e, e′, e″) Confocal fluorescence microscopy images of a p(VAc)$^+$/p(EtMA)$^-$ NP mixture at 10 °C (e), 22 °C (e′), and 80 °C (e″). In (d), (d′), (e), (e′), and (e″) the NP diameter was 400 nm. In all experiments $\varphi+/\varphi-$ = 1.0 and φ_{tot} = 0.15.

suggested that the gel had a weak order. The effect of increasing fractal dimensions at greater length scales for the colloidal gel (containing H-H contacts) was similar to that of the NP clusters assembled from hard NPs (Figure S6a, Supporting Information).

Colloidal interactions form hard−soft interparticle contacts. Since a marked difference was observed for NP mixtures with either solely H-H contacts or S-S contacts, in the next step, we explored the effect of hard−soft (H-S) NP contacts on the state of the system. A colloidal mixture was formed from anionic p(EtMa)$^-$ NPs (T_g = 75 °C) and cationic poly(vinyl acetate) NPs (pVAc)$^+$ NPs (T_g = 30 °C). The latter NPs had D_h = 60 ± 6 nm and ζ potential = |57 ± 7| mV (Figure S1, Supporting Information). A large difference in the T_g values of these counterpart NPs enabled experiments with H-H (at $T \leq$ 20 °C), H-S (15 $\leq T \leq$ 50 °C), and S-S (at $T \geq$ 75 °C) contacts, as illustrated in Figure 4a.

The structure of the NP clusters was explored by in situ SAXS experiments with a temperature ramp from 5 to 80 °C (Figure 4b). For this temperature interval, the power law features in the low q range of the SAXS intensity profiles changed the exponent α from 1.5 to 2.3 (Figure S6b, Supporting Information). At $T \leq$ 20 °C, the NP formed H-H contacts, and the resulting clusters had d_f = 1.5 (Figure 4b), similar to p(EtMA)$^+$/p(EtMA)$^-$ NP clusters formed below T_g (Figure 2c′). In the temperature range 20−30 °C (a glass transition region of p(VAc)), the NPs formed H-S contacts with a transition to aggregates with d_f = 2.3. The increase in the contact area from H-H to H-S contact was supported by the change in the form factor features in the high q range of the SAXS profiles (Figure S6c). Further increase in the temperature to 80 °C resulted in the formation of S-S contacts; however, no further change in d_f was observed.

These findings correlated with the results of rheology experiments carried out for the p(EtMA)$^-$/p(VAc)$^+$ NP mixture at 8 $\leq T \leq$ 80 °C. In this temperature range, a single transition from the gel state to the settling disconnected NP aggregates occurred at 30 °C, and the values of G' and G'' decreased from approximately 11000 to ∼1.0 Pa and from 3300 to ∼0.2 Pa, respectively (Figure 4c), with tan δ increasing from 0.30 to 0.50.

Figure 4d,d′,d″,e,e′,e′′ shows SEM and confocal fluorescence microscopy images of the mixture of (pVAc)$^+$/p(EtMa)$^-$ NPs at $\varphi+/\varphi-$ = 1.0 and φ_{tot} = 0.15. Hard NPs forming H-H contacts organized in a network comprised of fractal clusters (Figure 4d,e). The NP mixture with H-S contacts contained dense aggregates with partly merged NPs (Figure 4d′,e′). Following the transition to S-S contacts at 80 °C, the aggregate structure became more compact (Figure 4d″,e′′). Based on the results shown in Figure 4, we conclude that a symmetrical mixture of oppositely charged NPs undergoes NP aggregation, when at least one type of NPs is soft and forms H-S contacts with hard NPs.

The contribution of H-S contacts in the formation of discrete precipitating NP aggregates was further explored at φ_{tot} = 0.15 by varying the ratio between the volume fractions of cationic hard p(EtMA)$^+$ and soft p(VAc)$^+$ NPs, that is, φ_{H}+ and φ_{S}+, respectively, with a total ratio $\varphi+/\varphi-$ = 1.0. The volume fraction, φ_{H}-, of anionic hard p(EtMA) NPs was maintained at 0.5 (Figure 5a). First, a colloidally stable

https://doi.org/10.1021/acsnano.3c04064
ACS Nano 2023, 17, 15012−15024

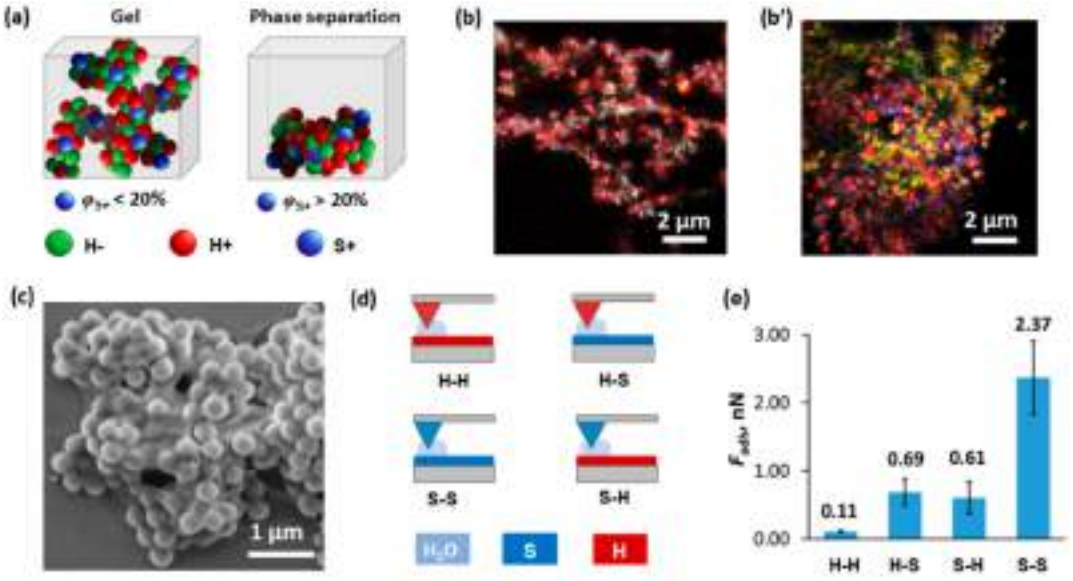

Figure 5. Contribution of soft NPs in the collapse of the colloidal gel. (a) Schematics of the formation of three-component gel (left) and NP aggregates (right) from hard anionic and hard cationic NPs, with the addition of soft cationic NPs at volume fraction φ_S+. (b, b′) Confocal fluorescence microscopy images of a p(VAc)$^+$/p(EtMA)$^+$/p(EtMA)$^-$ NP mixture formed at $\varphi_S+/\varphi_H+ = 0.25$ or $\phi_S+ = 10\%$ of φ_{tot} (b) and $\varphi_S+/\varphi_H+ = 0.67$ or $\varphi_S+ = 20\%$ of φ_{tot} (b′). p(EtMA)$^+$ NPs were labeled with Nile Red (λ_{em} = 630 nm), p(EtMA)$^-$ NPs were labeled with fluorescein acrylate (λ_{em} = 525 nm), and p(VAc)$^+$ NPs were labeled with vinyl anthracene (λ_{em} = 415 nm). (c) SEM image of three-component NP mixture as in (b′). (d) Illustration of AFM experiments. The tip and the substrate were covered with a hard (red color) or soft polymer (blue color). (e) Adhesion force measured between the polymer-coated AFM tip and the substrate.

dispersion of hard p(EtMA)$^+$ and soft p(VAc)$^+$ NPs at $0 \le \varphi_S+/\varphi_H+ \le 0.67$ was formed at 22 °C. Then, hard p(EtMA)$^-$ NPs were added to this dispersion to achieve volume ratio φ_S+/φ_{tot} in the range $0 \le \varphi_S+ \le 20\%$ of φ_{tot}.

A three-component colloidal gel formed at $\varphi_S+/\varphi_H+ < 0.5$ or $\varphi_S+ \le 15\%$ of φ_{tot}, while at $\varphi_S+/\varphi_H+ > 0.67$ or $\varphi_S+ \ge 20\%$ of φ_{tot} compact NP aggregates were formed (Figure 5b,b′, respectively). In the gel, soft NPs were uniformly distributed in the network (Figure 5b), while the aggregates exhibited structural inhomogeneity (Figure 5b′). An SEM image of the aggregate in Figure 5c reveals coalescence of soft NPs in the aggregate, while hard NPs present in excess attached to the surface of this aggregate.

In another experiment, we changed the order of mixing of oppositely charged hard and soft NPs. First, a colloidal gel was formed at φ_H- = 0.04 and φ_H+ = 0.03, that is, in excess of the anionic hard NPs. When cationic soft NPs were added to this gel at φ_S+/φ_H+ = 0.67 or φ_S+ 20% of φ_{tot}, significant precipitation of NP aggregates took place. Thus, we conclude that regardless of the order in which the oppositely charged NPs were mixed, the addition of soft NPs at a volume fraction as low as φ_S+ = 20% of φ_{tot} resulted in the collapse of the colloidal gel.

This result signifies the role of NP softness as an additional factor influencing interparticle interactions. To quantify this effect, we conducted atomic force microscopy (AFM) experiments to determine the adhesion force for H-H, H-S, and S-S polymer contacts. To mimic the formation of H-H, H-S, and S-S interparticle contacts, the AFM tip and the substrate were coated with p(EtMA)$^-$, p(EtMA)$^+$, p(VAc)$^+$, or p(VAc)$^-$ polymer (Figure 5d and Section S5, Supporting Information). For each type of contact, force−distance profiles were collected in water at 22 °C over an area of 1 μm × 1 μm. The adhesion force, F_{adh}, was calculated upon tip−surface separation from the adhesion peak in the retrace curve (Figure S8, Supporting Information). Figure 5e shows the magnitude of F_{adh} for H-H, H-S, S-H, and S-S contacts. The lowest adhesion force of 0.110 ± 0.014 nN was observed for H-H contacts formed by p(EtMA)$^-$ (tip) and p(EtMA)$^+$ (substrate). An approximately 6-fold higher adhesion force of 0.69 ± 0.19 nN was measured for the H-S contact formed by the p(EtMA)$^-$ (tip) and the p(VAc)$^+$ (substrate). A similar adhesion force of (0.61 ± 0.23) nN was measured between the tip coated with (p(VAc)$^+$ and the substrate covered with p(EtMA), which corresponded to an S-H contact. The largest F_{adh} of 2.37 ± 0.54 nN was measured for the S-S contact between p(VAc)$^+$ (tip) and p(VAc)$^-$ (substrate). These results signified the role of adhesion between H-S and, especially, S-S contacts in interparticle interactions.

An analysis of SEM images revealed that in the colloidal mixtures with H-H, H-S, and S-S contacts which were formed by 400 nm diameter NPs, the average interparticle distances were 381 ± 32, 331 ± 33 and 299 ± 21 nm; that is, a 13 and 22% decrease in the interparticle distance occurred for H-S and S-S contacts, respectively, in comparison with H-H contacts (Figure S9, in Supporting Information). For 60 nm diameter NPs, based on the results of SAXS experiments, the decrease in the interparticle distance for S-S contacts was 43%, in comparison with H-H contacts (Figure S6d, Supporting Information).

Modeling of Colloidal Interactions. We developed a phenomenological model to describe the interactions of oppositely charged NPs with different softnesses in molecular dynamics simulations. The details of the model are provided in Section S7, Supporting Information. The total interaction potential of spherical NPs interacting via soft and Coulomb potentials was modeled as

$$\beta u_{ij}(x) = \beta A\left(\frac{\sigma}{x}\right)^n + \frac{l_B}{\sigma}\frac{z_i z_j}{x} \quad (1)$$

https://doi.org/10.1021/acsnano.3c04064
ACS Nano 2023, 17, 15012−15024

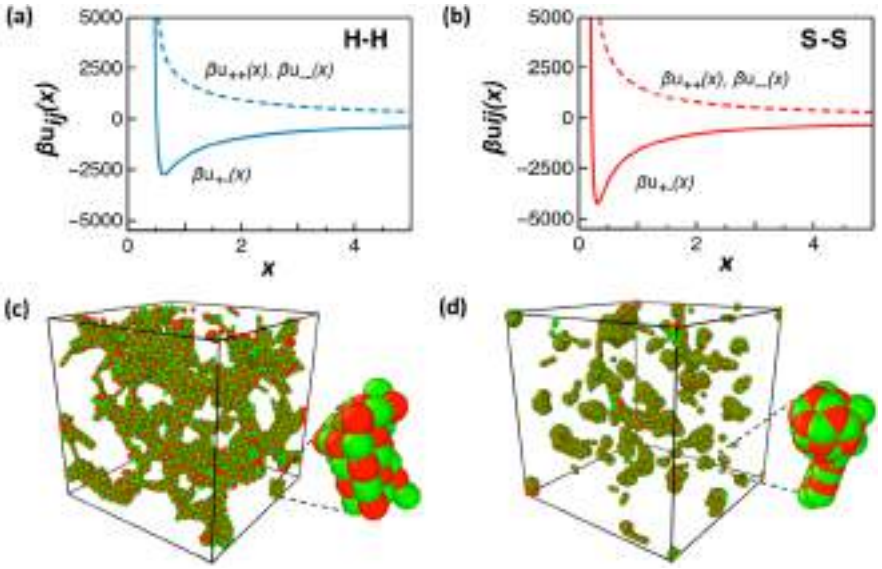

Figure 6. Simulations of interactions of hard and soft NPs. (a, b) Variation in the interaction potential with interparticle distance, plotted for hard NPs with H-H contacts (a) and soft NPs with S-S contacts (b). The top profiles (dashed lines) show repulsive interactions between likely charged NPs; the bottom profiles (the solid lines) show interactions between oppositely charged NPs. (c, d) Resulting nanostructures formed by hard NPs (c) and soft NPs (d). φ_{tot} = 0.15 and $\varphi+/\varphi-$ = 1.0.

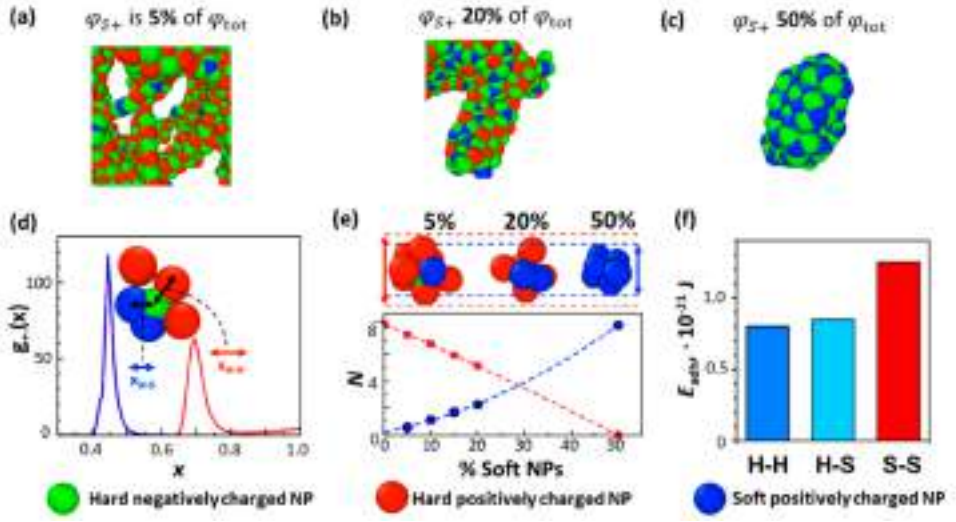

Figure 7. Simulations of mixtures formed by oppositely charged hard and soft NPs. (a–c) Snapshots of characteristic structures assembled upon mixing of negatively charged hard NPs at φ_H- = 0.075 and positively charged soft NPs at φ_S+ = 5% of φ_{tot} (a), 20% of φ_{tot} (b), and 50% of φ_{tot} (c). The total volume fraction cationic hard and soft NPs was 0.075. (d) Radial distribution functions for oppositely charged NPs: H-S interactions (blue profile) and H-H interactions (red profile) at φ_S+ = 20% of φ_{tot} (that is, φ_H- = 0.03). (e) The average number N of the nearest-neighbor cationic NPs around an anionic hard NP, plotted as a function of φ_{S+}. At the increasing φ_S+, the red square symbols represent the decrease in the number of hard NPs in a cluster and the blue circle symbols show the increase in the number of soft NPs in a cluster. The inset on the top of the graph shows representative structures with the nearest-neighbor positively charged NPs around a negatively charged hard NP. The red and blue vertical arrows show the dimensions of different clusters. (f) Cohesive energy for H-H, H-S, and S-S interactions. H-H and H-S contacts are modeled at T = 22 °C (<T_g); S-S contacts are modeled at T = 75 °C (T_g).

where $\beta = \frac{1}{k_B T}$, k_B is the Boltzmann constant, T is the temperature, x is the interparticle distance in units of the NP diameter σ at low T (σ = 400 nm), n is an exponent defining the "softness" of the repulsive part of the potential, z_i is the NP charge in units of e, i,j = (+,−) represent the positively and negatively charged NP, and l_B is the Bjerrum length given by $l_B = \frac{e^2}{4\pi\epsilon_0\epsilon_r k_B T}$, with ϵ_r being the relative dielectric constant of the solvent, ϵ_0 the dielectric permittivity of vacuum, and e the elementary charge. At $x_{min} = \left(\frac{\beta A n \sigma}{l_B |z_i z_j|}\right)^{1/n-1}$, oppositely charged NPs make contact and merge as T approaches T_g. Experimentally, it was observed that when the NPs were soft, the distance from their closest approach decreased. To reproduce this behavior, we set $A = \beta^{-1}$, which reflects the change in the interparticle distance (or the effective NP diameter) with temperature T via l_B, such that $x_{min} = \left(\frac{n\sigma}{l_B |z_i z_j|}\right)^{1/n-1}$ (see Figures S10–12, Supporting Informa-

https://doi.org/10.1021/acsnano.3c04064
ACS Nano 2023, 17, 15012–15024

tion). In mixtures of oppositely charged hard NPs (H-H contacts), the potential $\beta u_{ij}(x)$ includes the long-range Coulomb interactions and repulsive short-range interactions, which are represented by an inverse power low potential (IPL) and $n = 12$.[46] To model interactions of oppositely charged NPs with S-S contacts at $T = T_g$, we added soft attraction with a decay power law $n = 4$ to the repulsive IPL potential with $n = 6$, which describes the repulsion between soft particles[47] and the Coulomb interactions. Note that the theoretical model did not include gravity and hydrodynamic interactions, and the dynamics of the system were not described. We focused only the structure of the colloidal mixture, which is not strongly affected by hydrodynamics.[48]

Figure 6a,b shows the variation of the potential $\beta u_{ij}(x)$ vs interparticle distance x for the likely charged (dashed lines) and oppositely charged (solid lines) NPs forming H-H and S-S contacts, respectively, while the structures of the corresponding NP assemblies are shown in Figure 6c,d, respectively.

Clusters of hard NPs organized in a continuous 3D network (Figure 6c and Figure S13, Supporting Information), in which the NPs largely preserved their shape, while soft NPs formed discrete compact aggregates composed of deformed NPs with enlarged S-S contacts (Figure 6d and Figure S14, Supporting Information). These results correlated with the results of SEM and confocal microscopy imaging (Figure 3, respectively). The magnitude of the attractive potential in Figure 6a,b is significantly larger than the thermal energy k_BT. Most of this attraction originates from the large NP charge which affects their Coulombic interactions. A large value of the attractive potential is consistent with irreversible aggregation on a microscopic scale and strong polymer adhesion. Adhesion forces extracted from AFM experiments were 0.11 and 2.37 nN for H-H and S-S interactions, respectively, and in the simulations, the corresponding forces followed the same trend, that is, they are 0.044 and 0.2 nN (see details in the Supporting Information).

To explore the role of H-S contacts in the network formation, we modeled interactions in the mixture of anionic hard NPs at $\varphi_H- = 0.075$ (that is, half of $\varphi_{tot} = 0.15$) and cationic NPs with a varying fraction φ_S+ of soft NPs. Figure 7a−c shows the snapshots of molecular dynamic simulations of the mixture at φ_S+ of 5, 20, and 50% of φ_{tot}, respectively.

Figure 7d shows the radial distribution function $g_{(+-)}(x)$ for the clusters of oppositely charged NPs at $\varphi_S+ = 20\%$ of φ_{tot}. Due to the NP deformation, two peaks were observed in the distribution function: one at $x = 0.45$, corresponding to the distance between hard and soft NPs, that is, for H-S contacts (in units of the NP diameter $\sigma = 400$ nm), and another peak at $x = 0.71$, representing the distance between the hard NPs (H-H contacts). When φ_S+ increased from 20 to 50% of φ_{tot}, the peak corresponding to the H-H contacts disappeared, which indicated that soft NPs underwent local coalescence and the cluster became denser (Figure S15, Supporting Information).

Next, we modeled the average number N of the nearest-neighbor positively charged NPs around a hard negatively charged NP by computing the integral between two consecutive minima (distances r_1 and r_2) between H-S (blue) and H-H (red) in Figure 7d as $N = 24\varphi_{tot}\int_{r_1}^{r_2} g_{\pm}(x)x^2 dx$ (Figure 7e). The value of N was 0 and 2 for φ_S+ of 5 and 20% of φ_{tot}, respectively, which suggested that with increasing φ_S+, the interparticle distance in H-S contacts was smaller than that on H-H contacts. This effect indicated the tendency for suppressed gel formation in favor of compact clusters (aggregates) with an increasing fraction of soft NPs, in agreement with the trend in the variation of experimentally measured interparticle distances in the colloidal mixtures with H-H, H-S, and S-S contacts.

Finally, Figure 7f shows the cohesive energy for interactions of H-H, H-S, and S-S NPs. This energy is substantially larger for S-S than for H-H contacts, indicating that more energy is needed to separate a pair of oppositely charged soft NPs than hard NPs.[49] Since the cohesive energy is associated with adhesion between polymer surfaces, these results support the AFM results obtained for H-H, H-S, and S-S polymer contacts (Figure 5e).

DISCUSSION

In the present work, mixing of positively and negatively charged NPs resulted in spinodal decomposition of the binary colloidal mixture, as has been established for the mixtures of oppositely charged latex and inorganic particles.[50−52] As a result of instability, density fluctuations in the colloid-rich phase favored attraction between the oppositely charged NPs. Hard NPs formed H-H interparticle contacts in which the NPs were not deformed. These NPs assembled in open clusters with fractal dimensions in the range of 1.5−1.9 (determined by image analysis, SLS, SAXS, and rheology experiments), in agreement with earlier reports on clusters formed by attractive hard colloids.[14,50] Importantly, close correlation was observed between the results of SAXS and SLS for clusters of NPs with more than a 6-fold difference in NP dimensions.

When the overall volume fraction, φ_{tot}, of hard NPs exceeded a threshold value, the growing clusters formed a kinetically arrested space-spanning network with a uniform distribution of oppositely charged NPs. Due to the "symmetry" of counterpart NPs, the gel region in the state diagram of the colloidal mixture was symmetrical with respect to the volume fractions of oppositely charged NPs. Gel formation was presumably governed by DLCA, although based on the relatively low value of the adhesive force for H-H contacts (Figure 5d), the contribution of RLCA cannot be ignored. The mechanism of colloidal gel formation was distinct from thermodynamically driven assembly of colloidal crystals from oppositely charged particles.[53]

Clusters and network formation were qualitatively similar for oppositely charged NPs with dimensions in the range from 60 to 400 nm. The experimental results, including the decrease in interparticle distance from H-H to H-S to S-S contacts, were in agreement with the trend in the variation of experimentally measured interparticle distances in the colloidal mixtures with H-H, H-S, and S-S contacts. We note in our experiments that NP density did not match the density of the surrounding liquid; however, based on previous experimental evidence in studies of network formation from significantly larger colloids,[50] gravity had a weak effect on the gel structure.

At the same threshold value of φ_{tot} that resulted in the formation of a colloidal gel from hard NPs, a binary mixture of oppositely charged soft NPs broke up into discrete, dense aggregates. These NPs interacted via long-range Coulomb interactions and repulsive short-range interactions, with a significant contribution of the soft potential (exponents decreasing as the temperature increased), consistent with interactions of soft NPs. The NPs in this mixture formed S-S contacts, for which the adhesive force was approximately 20-fold higher than for H-H contacts. A large adhesive force led to

https://doi.org/10.1021/acsnano.3c04064
ACS Nano 2023, 17, 15012−15024

an increased contact area between the deformed soft NPs, irreversible contacts between the same-charge soft NPs, and a nonuniform distribution of soft NPs in the aggregates, as shown in the images in Figures 2 and 3. Moreover, since soft NPs were not cross-linked, at the temperature above polymer T_g, they ultimately underwent coalescence to reduce the surface free energy of the system. For two coalescing NPs, the reduction of the surface energy was $\Delta E_{st} = \sigma \Delta A$, where σ is the temperature-dependent interfacial tension between the NP and the surrounding liquid and ΔA is the change in the area of the NP-NP interface when two NPs undergo coalescence. The resulting dense aggregates of soft NPs expelled water and rapidly precipitated, although due to the NP deformation, these aggregates were smaller than clusters of hard NPs. Owing to the large adhesive force and NP coalescence, the formation of discrete NP aggregates in the mixture of soft NPs was irreversible. We note that in the control experiments, phase separation in the colloidal system occurred when NP coalescence was suppressed. At φ_{tot} = 0.15, a symmetrical mixture of $p(VAc)^+$ and $p(VAc)^-$ NPs weakly cross-linked with 0.5 mol % of the cross-linking agent exhibited strong aggregation at 22 °C, while a colloidal gel formed at 5 °C (Figure S16, Supporting Information).

Interactions in mixtures of oppositely charged hard and soft NPs were the most interesting case. A single transition from the colloidal gel to discrete aggregates in the binary NP mixture was caused by the formation of H-S contacts with an intermediate, yet high, value of the adhesive force (Figure 5c). Based on the results of simulations, due to an increased area of contact between the soft and hard NPs, hard NPs had a larger number of soft nearest neighbors than in the case of H-H contacts (Figure 7d,e), which led to the formation of dense aggregates. The collapse of the colloidal gel occurred at the volume fraction of soft NPs as small φ_S+ = 20% of φ_{tot}, signifying the importance of H-S interactions. Over a prolonged time, aggregate precipitation was followed by the coalescence of soft $p(VAc)^+$ NPs, as well as the engulfment of hard $p(EtMA)^-$ NPs with the pVAc polymer.

We stress that due to the high polymer viscosity at the temperature above T_g,[54] spreading and coalescence of p(VAc) would require substantial time, while the formation of rapidly precipitating discrete NP aggregates at φ_S+ exceeding 20% occurred almost immediately after NP mixing. We conclude that on a short time scale that this effect was the result of soft NP collisions and instantaneous NP deformation, resulting in an increased number of soft nearest neighbors and the formation of dense settling aggregates, rather than polymer spreading and coalescence. This conclusion is also supported by the observed changes of the form factor features in the high-q range of SAXS intensity profiles, as well as SAXS simulations (Figure S6b,c). At a sufficient time after mixing of soft and hard NPs, a direct analogy existed between the colloidal mixtures with H-S contacts described above and the result of adding a small amount of the second particle-wetting liquid to the original particle dispersion.[55] In the latter system, capillary liquid bridges forming between the solid particles lead to attractive capillary forces of the two fluids and cause a liquid-to-gel transition or a transition from a weak to a strong gel.[56] Similarly, in our work, at a prolonged time after NP mixing, coalescence and spreading of soft NPs may result in capillary bridges leading to attractive capillary forces between the hard NPs.

We stress the difference between interactions of oppositely charged hard and soft latex NPs in our work and in the mixtures of branched star polymers with long and short arms, which were used as model systems of soft and hard spheres, respectively.[57] In the latter system, the governing factors of the appearance of multiple phases and reversible transitions between them were the softness of the star polymer NPs, the size ratio of soft and hard NPs, and their osmotic shrinkage. In the binary NP system studied in the present work, the colloidal mixture was symmetrical with respect to the NP dimensions, and the NPs were not permeable. Instead, deformation of soft NPs in interparticle contacts led to an increased number of soft neighbors around hard NPs and was the driving force for cluster densification and precipitation, which led to an irreversible collapse of the colloidal gel.

The experimental results were in agreement with the phenomenological model and molecular dynamics simulations of oppositely charged NPs interacting via soft and Coulomb potentials. The model described colloidal interactions with the formation of H-H, S-S, and H-S contacts, the structure of gels (that is, the number of nearest neighbors), and the cohesive energy of the NPs in S-S, H-S, and H-H contacts (we note that due to the contact geometry in the AFM experiments we have chosen adhesion as the descriptor, while cohesion was appropriate for the simulations. As such, the model enabled the prediction of the structure of colloidal clusters and networks formed by NPs with different stiffnesses.

CONCLUSIONS

Experimental and simulation studies of interactions in mixtures of oppositely charged polymer NPs with similar dimensions, symmetrical opposite charges, and different softnesses provided insight into the role of hard−hard, hard−soft, and soft−soft interparticle contacts in the formation of colloidal clusters and gels. We show that oppositely charged hard NPs assemble in open clusters with fractal dimensions in the range of 1.5−1.9. The growing clusters of hard NPs form a kinetically arrested space-spanning reversible colloidal gel. In contrast, colloidal interactions in the mixture of oppositely charged soft NPs result in the formation of dense precipitating aggregates and phase separation. A large adhesive force between the soft NPs results in irreversible contacts between both same-charge and oppositely charged NPs, an increased contact area between the NPs, due to their deformation, and a nonuniform distribution of soft NPs in the aggregates. Ultimately, soft NPs in the aggregates undergo coalescence.

We show that a transition from the colloidal gel to discrete precipitating aggregates occurs at a relatively small (20%) volume fraction of soft NPs in the stoichiometric mixture of oppositely charged NPs. This result highlights the importance of hard−soft interactions with an intermediate value of the adhesive interparticle force.

Our findings provide an alternative mechanistic insight in the field of colloid science by broadening our understanding of particle interactions and network formation via an appreciation of the role of contact mechanics in colloidal mixtures. Currently, condensed particles are predominantly viewed as hard spheres, and the effect of a contact area change on particle interactions due to particle softness is largely neglected. Our results for mixtures of condensed hard−soft particles show how sensitive colloidal interactions and colloidal network formation are to very small changes in contact mechanics of the particles, a phenomenon that cannot be explained by well-

https://doi.org/10.1021/acsnano.3c04064
ACS Nano 2023, 17, 15012−15024

established theoretical descriptions of colloidal systems. Moreover, since kinetically arrested colloidal gels have applications in the food industry, personal care products, water purification, biotechnologies, aerogel preparation, and extrusion-based 3D printing, our findings have far-reaching implications for the design of materials used in these technologies.

MATERIALS AND METHODS

Nanoparticle Synthesis and Characterization. Synthesis of latex NPs was carried out using a modified a semicontinuous "seed-and-feed" procedure reported elsewhere.[1] The recipes for NP synthesis are provided in Table S1 in the Supporting Information. Following NP synthesis, the dispersion was placed in the dialysis bag (a membrane cutoff of 14000) and dialyzed against deionized water for 1 week with water changes every 24 h.

To perform confocal microscopy imaging, the NPs were labeled with fluorescent dyes. The $p(VAc)^+$, $p(EtMA)^+$, and $p(EtMA)^-$ NPs were labeled with 9-vinyl anthracene, Nile Red, and fluorescein acrylate, respectively. Fluorescein acrylate or 9-vinyl anthracene was dissolved in acetone, while Nile Red was dissolved in hexane to form a 1 wt % solution. The dispersion of 400 nm $p(VAc)^+$, $p(EtMA)^+$, or $p(EtMA)^-$ NPs was diluted to φ_{tot} = 0.05 and mixed with a corresponding dye solution in a volume ratio of latex NP dispersion to dye solution of 10:1. Fluorescence of dye-labeled latex NPs was examined using a spectrofluorimeter (Varian, CA, USA). The excitation wavelengths were 390, 488, and 550 nm for the NPs labeled with vinyl anthracene, fluorescein acrylate, and Nile Red, respectively.

The hydrodynamic diameter and ζ potential of the NPs were determined using a Malvern Zetasizer Nano ZS, Model ZEN3600. The data were analyzed by the Malvern General Purpose non-negative least-squares method.

Differential scanning calorimetry experiments were performed in an argon atmosphere on a NETZSCH DSC 204 F1 Phoenix calorimeter. The temperature was changed from 0 to 150 °C with a heating rate of 5 °C/min. The glass transition temperature of the polymer was determined using NETZSCH Proteus Thermal Analysis Version 6.1.0 software.

Studies of Cluster and Gel Formation. Individual aqueous dispersions of oppositely charged NPs at the temperature in the range from 10 to 80 °C were mixed by vortexing for 30 s and maintained at the designated temperature for 20 min. Flip tests were performed to evaluate the state of the NP mixture.

Scanning electron microscopy (SEM) imaging of gels and NP clusters was carried out at 3−5 kV using a Quanta FEI scanning electron microscope. A cooling stage was used to perform imaging at −15 °C to prevent NP coalescence, which was caused by heating with the electron beam. Confocal microscopy imaging of NP clusters and gels was performed on a Leica SP8 microscope (PMCRT 15-605) with an oil immersion lens at 63× magnification. For gel imaging, an IBIDI uncoated cell (IBIDI, Germany) with 8 channels and 2 μm height was used. For NP clusters, imaging was performed using an eight-well chambered cover glass. Fractal analysis of confocal microscopy and SEM images of NP clusters was carried out by the box counting method, using FracLac plugin for ImageJ software.[38] The minimum size of the grid was set to be equal to four diameters of individual NPs. Four different images were analyzed to obtain the fractal dimensions of clusters. Each image contained approximately 10000 NPs.

Rheology experiments were performed on a plate−plate rheometer (AR-1000 TA Instruments) with a 40 mm diameter plate. A solvent trap was utilized to minimize the solvent evaporation. Temperature ramp experiments were performed in the temperature range from 20 to 80 °C for p(EtMA) NP-based gel and from 10 to 40 °C for p(EtMA)/p(VAc) gel at a strain of 0.5% and a frequency of 1 Hz, with 10 min equilibration of the sample at each temperature. The temperature dependence of the storage and loss moduli, G' and G'', respectively, of the gels prepared at a particular temperature was determined at a strain of 0.5% and a frequency of 1 Hz with 10 min equilibration time at each temperature. Oscillation strain tests at a frequency of 1.5 Hz were performed at 22 °C using a DH-R Rheometer TA Instruments with a 40 mm flat geometry to determine the fractal dimension of the gels.

Small-angle X-ray scattering (SAXS) experiments were carried out at the Complex Materials Scattering (CMS, 11-BM) beamline at the National Synchrotron Light source II (NSLS-II) at Brookhaven National Laboratory (BNL). An X-ray beam with a photon energy of E = 13.5 keV was used, and the scattering was collected by a 2D detector (Pilatus 2M, 172 × 172 μm^2 per pixel) with a sample-to-detector distance of 5 m.

Static light scattering (SLS) measurements were performed using a BI-200SM Research Goniometer System at Brookhaven Instruments. A laser (λ = 640 nm) was used to illuminate the sample in a 20 mL round glass cell. The scattering intensity was collected at scattering angles varying from 9 to 155°. The q range was 0.0002−0.0025 $Å^{-1}$, which corresponded to a length scale of 250 nm to 3 μm. The intensity profile for each sample was an average of three measurements.

Measurements of Interparticle Distance. For 400 nm NPs, the average center-to-center interparticle distance in mixtures with H-H, H-S, and S-S contacts was determined by analyzing their SEM images using ImageJ software (NIH). For H-H, H-S, and S-S contacts, 30, 30, and 20 measurements were performed, respectively. The distance between 60 nm NPs was determined in SAXS experiments. In the H-H system, the average distance between the neighboring NPs was taken as corresponding to a diameter of the hard NP. For the S-S contacts, to estimate an average interparticle distance, we fitted the SAXS data in the high-q range by a dumbbell model of form factor for touching spheres (see details in the Supporting Information).

Atomic Force Microscopy Experiments. AFM studies were performed using an MFP-3D-BIO Asylum research microscope (Oxford Instruments, Santa Barbara, CA, USA). The spring constants of the silicon nitride AFM probes (Bruker's DNP) were ∼50 pN/nm after coating them with a polymer. The uncoated tips had apexes with nominally a 20 nm radius of curvature. Experiments were conducted by introducing a droplet of deionized water (18 mΩ) between the polymer-coated AFM tip and the polymer surface. The tip was modified by immersing it in the polymer solution in dichloromethane (0.005 wt % concentration). Respective polymer dispersions containing $p(EtMA)^+$, $p(EtMa)^-$, $p(VAc)^-$ and $p(VAc)^+$ NPs were dried and dissolved in dichloromethane. A glass slide was coated with a polymer by spin-coating a 1.0 wt % polymer solution in dichloromethane at 2500 rpm for 60 s. The polymer-coated AFM tip was brought in contact with the polymer-coated substrate under water at a speed of 1 μm/s and retracted at a trigger set point (voltage of 1 V).

ASSOCIATED CONTENT

Supporting Information

The Supporting Information is available free of charge at https://pubs.acs.org/doi/10.1021/acsnano.3c04064.

Additional experimental details including latex NP detailed synthesis description, NP size distribution obtained by using dynamic light scattering, differential scanning calorimetry of latex NPs, size and electrokinetic potential for latex NPs at different temperatures, rheology data, phase diagrams for NPs with diameters of 60 and 150 nm, confocal microscopy for individual latex NPs, SAXS data, rheology data for calculation of fractal dimension of NP-based gels, atomic force microscopy data, measurements of interparticle distance based on SEM images, simulations details, and images of gelation and aggregation of slightly cross-linked NPs (PDF)

https://doi.org/10.1021/acsnano.3c04064
ACS Nano 2023, 17, 15012−15024

AUTHOR INFORMATION

Corresponding Authors

Monica Olvera de la Cruz − *Department of Materials Science and Engineering, Northwestern University, Evanston, Illinois 60208, United States; Department of Chemistry, Northwestern University, Evanston, Illinois 60208, United States;* orcid.org/0000-0002-9802-3627; Email: m-olvera@northwestern.edu

Eugenia Kumacheva − *Department of Chemistry, University of Toronto, Toronto M5S 3H6 Ontario, Canada; Institute of Biomaterials and Biomedical Engineering and Department of Chemical Engineering and Applied Chemistry, University of Toronto, Toronto M5S 3H6 Ontario, Canada;* orcid.org/0000-0001-5942-3890; Email: eugenia.kumaheva@utoronto.ca

Authors

Sofia M. Morozova − *Department of Chemistry, University of Toronto, Toronto M5S 3H6 Ontario, Canada;* orcid.org/0000-0001-8680-3653

Leticia López-Flores − *Department of Materials Science and Engineering, Northwestern University, Evanston, Illinois 60208, United States;* orcid.org/0000-0003-0980-5537

Albert Gevorkian − *Department of Chemistry, University of Toronto, Toronto M5S 3H6 Ontario, Canada*

Honghu Zhang − *Center for Functional Nanomaterials, Brookhaven National Laboratory, Upton, New York 11973, United States; National Synchrotron Light Source II, Brookhaven National Laboratory, Upton, New York 11973, United States;* orcid.org/0000-0003-1784-7825

Vahid Adibnia − *Department of Chemistry, University of Toronto, Toronto M5S 3H6 Ontario, Canada;* orcid.org/0000-0001-9006-8137

Weiqing Shi − *Department of Chemistry, University of Toronto, Toronto M5S 3H6 Ontario, Canada*

Dmytro Nykypanchuk − *Center for Functional Nanomaterials, Brookhaven National Laboratory, Upton, New York 11973, United States*

Tatiana G. Statsenko − *Department of Chemistry, University of Toronto, Toronto M5S 3H6 Ontario, Canada;* orcid.org/0000-0001-9282-547X

Gilbert C. Walker − *Department of Chemistry, University of Toronto, Toronto M5S 3H6 Ontario, Canada;* orcid.org/0000-0002-5248-5498

Oleg Gang − *Center for Functional Nanomaterials, Brookhaven National Laboratory, Upton, New York 11973, United States; Departments of Chemical Engineering and Applied Physics and Applied Mathematics, Columbia University, New York, New York 10027, United States;* orcid.org/0000-0001-5534-3121

Complete contact information is available at: https://pubs.acs.org/10.1021/acsnano.3c04064

Author Contributions

S.M.M. and L.L.-F. contributed equally. E.K. and S.M.M. designed the project. S.M.M., A.G., and V.A. synthesized latex NPs, performed their characterization, and constructed phase diagrams. T.G.S. carried out DSC analysis. A.G. and S.M.M. carried out rheology experiments. S.M.M. performed confocal microscopy imaging and determined fractal dimensions based on rheology and image analysis data. O.G., H.Z., and D.N. carried out and analyzed SAXS and SLS profiles and determined fractal dimensions. W.S. and G.C.W. performed atomic force microscopy experiments and analyzed the results. L.L.-F. and M.O.d.l.C. developed the theoretical framework and performed modeling of the behavior of colloidal mixtures. The manuscript was written through contributions of all authors. All authors have given approval to the final version of the manuscript.

Funding

E.K. and G.C.W. are grateful to NSERC Canada for financial support of this work by the Discovery program. The work of L.L-F. and M.O.d.l.C. was supported by the NSF Center for the Chemistry of Molecularly Optimized Networks (MONET), CHE-2116298. H.Z., D.N., and O.G. used the Material Synthesis and Characterization facility of the Center for Functional Nanomaterials at Brookhaven National Laboratory, supported by the U.S. DOE Office of Science, under Contract No. DE-SC0012704. Small angle X-ray scattering was collected at the Complex Matter Scattering (CMS) 11-BM beamline of the National Synchrotron Light Source II at Brookhaven National Laboratory, which is a U.S. DOE Office of Science User Facility (Contract No. DE-SC0012704).

Notes

The authors declare no competing financial interest.

ACKNOWLEDGMENTS

The authors thank James Jonkman (University Health Network, Toronto) and Ilya Gourevich (University of Toronto) for assistance in imaging experiments and Esther Tsai (Brookhaven National Laboratory) for assistance in SAXS experiments. H.Z., D.N., and O.G. acknowledge Brookhaven Instruments for providing a research platform for static light scattering (SLS) and thank Daniel Napolitano and Daniel Seeman for assistance of the SLS experiments.

ABBREVIATIONS

AFM, atomic force microscopy; CMS, complex matter scattering; DLS, dynamic light scattering; DSC, differential scanning calorimetry; H-H, hard−hard contacts; H-S, hard−soft contacts; NPs, nanoparticles; p(EtMA), poly(ethyl methacrylate); p(VAc), poly(vinyl acetate); SAXS, small-angle X-ray scattering; SEM, scanning electron microscopy; SLS, static light scattering; S-S, soft−soft contacts

REFERENCES

(1) Packham, D. E. *Handbook of Adhesion*; John Wiley & Sons: 2006.

(2) Qin, Y. F.; Fichthorn, K. A. Solvation forces between colloidal nanoparticles: directed alignment. *Phys. Rev. E* **2006**, *73*, 020401.

(3) Leong, Y. K.; Boger, D. V.; Scales, P. J.; Healy, T. W.; Buscall, R. Control of the rheology of concentrated aqueous colloidal systems by steric and hydrophobic forces. *Chem. Commun.* **1993**, *7*, 639−641.

(4) Smalley, M. V. Electrostatic interaction in macro-ionic solutions and gels. *Mol. Phys.* **1990**, *71*, 1251−1267.

(5) Mao, Y.; Cates, M. E.; Lekkerkerker, H. N. W. Depletion force in colloidal systems. *Phys. A Stat. Mech. its Appl.* **1995**, *222*, 10−24.

(6) Dai, L.; Sun, C.; Wei, Y.; Mao, L.; Gao, Y. Characterization of Pickering emulsion gels stabilized by zein/gum arabic complex colloidal nanoparticles. *Food Hydrocoll.* **2018**, *74*, 239−248.

(7) Doost, A. S.; Nasrabadi, M. N.; Kassozi, V.; Nakisozi, H.; Van der Meeren, P. Recent advances in food colloidal delivery systems for essential oils and their main components. *Trends Food Sci. Technol.* **2020**, *99*, 474−486.

(8) Sonia, S.; Ruckmani, K.; Sivakumar, M. Antimicrobial and antioxidant potentials of biosynthesized colloidal zinc oxide nano-

particles for a fortified cold cream formulation: A potent nano-cosmeceutical application. *Mater. Sci. Eng., C* **2017**, *79*, 581−589.
(9) Tomczyk, W.; Longa, L.; Zion, M. Y. B.; Caba, Y.; Sha, R.; Seeman, N. C.; Chaikin, P. M. Where physics meets chemistry meets biology for fundamental soft matter research. *Soft Matter* **2020**, *16*, 4343−4349.
(10) Hou, Y.; Jiang, N.; Zhang, L.; Li, Y.; Meng, Y.; Han, D.; Chen, Y.; Yang, Y.; Zhu, S. Oppositely charged polyurethane microspheres with tunable zeta-potentials as an injectable dual-loaded system for bone repair. *ACS Appl. Mater. Interfaces* **2017**, *9*, 25808−25817.
(11) Lam, S.; Velikov, K. P.; Velev, O. D. Pickering stabilization of foams and emulsions with particles of biological origin. *Curr. Opin. Colloid Interface Sci.* **2014**, *19*, 490−500.
(12) Morozova, S. M.; Statsenko, T. G.; Ryabchenko, E. O.; Gevorkian, A.; Adibnia, V.; Lozhkin, M. S.; Kireynov, A. V.; Kumacheva, E. Multicolored nanocolloidal hydrogel inks. *Adv. Funct. Mater.* **2021**, *31* (1−8), 2105470.
(13) Zeng, M.; Zhang, Y. Colloidal nanoparticle inks for printing functional devices: emerging trends and future prospects. *J. Mater. Chem. A* **2019**, *7*, 23301−23336.
(14) Russell, E. R.; Sprakel, J.; Kodger, T. E.; Weitz, D. A. Colloidal gelation of oppositely charged particles. *Soft Matter* **2012**, *8*, 8697−8703.
(15) Keshavarz, B.; Rodrigues, D. G.; Champenois, J. B.; Frith, M. G.; Ilavsky, J.; Geri, M.; Divoux, T.; McKinley, G. H.; Poulesquen, A. Time-connectivity superposition and the gel/glass duality of weak colloidal gels. *Proc. Natl. Acad. Sci. U.S.A.* **2021**, *118*, No. e2022339118.
(16) Lin, M. Y.; Lindsay, H.; Weitz, D. A.; Ball, R. C.; Klein, R.; Meakin, P. Universality in colloid aggregation. *Nature* **1989**, *339*, 360−362.
(17) Berg, J. C. An introduction to Interfaces and Colloids: the Bridge to Nanoscience, World Scientific, 2010.
(18) Zaccarelli, E. Colloidal gels: equilibrium and non-equilibrium routes. *J. Phys.: Condens. Matter* **2007**, *19*, 323101.
(19) Sanz, E.; Valeriani, C.; Vissers, T.; Fortini, A.; Leunissen, M. E.; Van Blaaderen, A.; Frenkel, M.; Dijkstra, M. Out-of-equilibrium processes in suspensions of oppositely charged colloids: liquid-to-crystal nucleation and gel formation. *J. Phys.: Condens. Matter* **2008**, *20*, 494247.
(20) Sciortino, F.; Zaccarelli, E. Equilibrium gels of limited valence colloids. *Curr. Opin. Colloid Interface Sci.* **2017**, *30*, 90−96.
(21) Vinutha, H. A.; Frenkel, D. Estimation of the equilibrium free energy for glasses using the Jarzynski equality. *J. Chem. Phys.* **2021**, *154*, 231101.
(22) Nykypanchuk, D.; Maye, M. M.; Van Der Lelie, D.; Gang, O. DNA-guided crystallization of colloidal nanoparticles. *Nature* **2008**, *451*, 549−552.
(23) Lu, P. J.; Weitz, D. A. Colloidal particles: Crystals, glasses, and gels. *Annu. Rev. Condens. Matter Phys.* **2013**, *4*, 217−233.
(24) Spruijt, E.; Bakker, H. E.; Kodger, T. E.; Sprakel, J.; Stuart, M. A. C.; van der Gucht, J. Reversible assembly of oppositely charged hairy colloids in water. *Soft Matter* **2011**, *7*, 8281−8290.
(25) Mohraz, A.; Weeks, E. R.; Lewis, J. A. Structure and dynamics of biphasic colloidal mixtures. *Phys. Rev. E* **2008**, *77*, 060403.
(26) Ruiz-Franco, J.; Zaccarelli, E. On the role of competing interactions in charged colloids with short-range attraction. *Annu. Rev. Condens. Matter Phys.* **2021**, *12*, 51−70.
(27) Demirörs, A. F.; Stiefelhagen, J. C.; Vissers, T.; Smallenburg, F.; Dijkstra, M.; Imhof, A.; Van Blaaderen, A. Long-ranged oppositely charged interactions for designing new types of colloidal clusters. *Phys. Rev. X* **2015**, *5*, 1−12.
(28) van Schooneveld, M. M.; de Villeneuve, V. W.; Dullens, R. P. A.; Aarts, D. G.; Leunissen, M. E.; Kegel, W. K. Structure, stability, and formation pathways of colloidal gels in systems with short-range attraction and long-range repulsion. *J. Phys. Chem. B* **2009**, *113*, 4560−4564.
(29) van der Linden, E.; Foegeding, E. A. Gelation: principles, models and applications to proteins. *Modern biopolymer science*; Academic Press: 2009.
(30) Style, R. W.; Hyland, C.; Boltyanskiy, R.; Wettlaufer, J. S.; Dufresne, E. R. Surface tension and contact with soft elastic solids. *Nat. Commun.* **2013**, *4*, 2728.
(31) Schulte, M. F.; Izak-Nau, E.; Braun, S.; Pich, A.; Richtering, W.; Göstl, R. Microgels react to force: mechanical properties, syntheses, and force-activated functions. *Chem. Soc. Rev.* **2022**, *51*, 2939−2956.
(32) Richtering, W.; Saunders, B. R. Gel architectures and their complexity. *Soft Matter* **2014**, *10*, 3695.
(33) Biesheuvel, P. M.; Lindhoud, S.; Stuart, M. A. C.; de Vries, R. Phase behavior of mixtures of oppositely charged protein nanoparticles at asymmetric charge ratios. *Phys. Rev. E - Stat. Nonlinear, Soft Matter Phys.* **2006**, *73*, 041408.
(34) Ninarello, A.; Crassous, J. J.; Paloli, D.; Camerin, F.; Gnan, N.; Rovigatti, L.; Schurtenberger, P.; Zaccarelli, E. Modeling microgels with a controlled structure across the volume phase transition. *Macromolecules* **2019**, *52*, 7584−7592.
(35) Mohanty, P. S.; Paloli, D.; Crassous, J. J.; Zaccarelli, E.; Schurtenberger, P. Effective interactions between soft-repulsive colloids: experiments, theory, and simulations. *Nat. Commun.* **2018**, *9*, 1−11.
(36) Mohanty, P. S.; Paloli, D.; Crassous, J. J.; Zaccarelli, E.; Schurtenberger, P. Effective interactions between soft-repulsive colloids: experiments, theory, and simulations. *J. Chem. Phys.* **2014**, *140*, 094901.
(37) Eggersdorfer, M. L.; Pratsinis, S. E. Agglomerates and aggregates of nanoparticles made in the gas phase. *Adv. Powder Technol.* **2014**, *25*, 71−90.
(38) Nayak, S. R.; Mishra, J. Fractal dimension-based generalized box-counting technique with application to grayscale images. *Fractals* **2021**, *29*, 2150055.
(39) Shih, W. H.; Shih, W. Y.; Kim, S. I.; Liu, J.; Aksay, I. A. Scaling behavior of the elastic properties of colloidal gels. *Phys. review A* **1990**, *42*, 4772.
(40) Pfeifer, D. J.; Ehrburger-Dolle, P.; Rieker, F.; González, T. P.; Hoffman, M. T.; Molina-Sabio, M.; Rodríguez-Reinoso, F.; Schmidt, P. W.; Voss, D. J. Nearly space-filling fractal networks of carbon nanopores. *Phys. Rev. Lett.* **2002**, *88*, 115502.
(41) Cherny, A. I.; Anitas, A. Y.; Osipov, E. M.; Kuklin, V. A. Scattering from surface fractals in terms of composing mass fractals. *J. Appl. Crystallogr.* **2017**, *50*, 919−931.
(42) Glatter, O. *Scattering methods and their application in colloid and interface science*; Elsevier: 2018.
(43) Kao, P. K.; Solomon, M. J.; Ganesan, M. Microstructure and elasticity of dilute gels of colloidal discoids. *Soft Matter* **2022**, *18*, 1350−1563.
(44) Schaefer, D. W.; Rieker, T.; Agamalian, M.; Lin, J. S.; Fischer, D.; Sukumaran, S.; Chen, C.; Beaucage, G.; Herd, J.; Ivie, J. Multilevel structure of reinforcing silica and carbon. *J. Appl. Crystallogr.* **2000**, *33*, 587−591.
(45) Hansen, J. P.; McDonald, I. R. *Theory of Simple Liquids*; Academic Press: 1976.
(46) Ben-Amotz, D.; Stell, G. Hard sphere perturbation theory for fluids with soft-repulsive-core potentials. *J. Chem. Phys.* **2004**, *120*, 4844−4851.
(47) Lipkowitz, K. B.; Boyd, D. B. *Reviews in computational chemistry 7*; Wiley: 1996.
(48) Kovalchuk, N. M.; Starov, V. M. Aggregation in colloidal suspensions: effect of colloidal forces and hydrodynamic interactions. *Adv. Colloid Interface Sci.* **2012**, *179*, 99−106.
(49) Campos-Villalobos, G.; Boattini, E.; Filion, L.; Dijkstra, M. Machine learning many-body potentials for colloidal systems. *J. Chem. Phys.* **2021**, *155*, 174902.
(50) Lu, P. J.; Zaccarelli, E.; Ciulla, F.; Schofield, A. B.; Sciortino, F.; Weitz, D. A. Gelation of particles with short-range attraction. *Nature* **2008**, *453*, 499−503.

https://doi.org/10.1021/acsnano.3c04064
ACS Nano 2023, 17, 15012−15024

(51) Yethiraj, A.; van Blaaderen, A. A colloidal model system with an interaction tunable from hard sphere to soft and dipolar. *Nature* **2003**, *421*, 513−517.
(52) Poulin, P.; Bibette, J.; Weitz, D. A. From colloidal aggregation to spinodal decomposition in sticky emulsions. *Eur. Phys. J. B-Condensed Matter Complex Syst.* **1999**, *7*, 277−281.
(53) Parisi, D.; Camargo, M.; Makri, K.; Gauthier, M.; Likos, C. N.; Vlassopoulos, D. Effect of softness on glass melting and re-entrant solidification in mixtures of soft and hard colloids. *J. Chem. Phys.* **2021**, *155*, 034901.
(54) Shenoy, A. V.; Saini, D. R. Melt flow index: More than just a quality control rheological parameter. *Adv. Polym. Technol.* **1986**, *6*, 1−58.
(55) Koos, E.; Willenbacher, N. Capillary forces in suspension rheology. *Science* **2011**, *331*, 897−900.
(56) Koos, E. Capillary suspensions: Particle networks formed through the capillary force. *Curr. Opin. Colloid Interface Sci.* **2014**, *19*, 575−584.
(57) Lazzari, S.; Nicoud, L.; Jaquet, B.; Lattuada, M.; Morbidelli, M. Fractal-like structures in colloid science. *Adv. Colloid Interface Sci.* **2016**, *235*, 1−13.

https://doi.org/10.1021/acsnano.3c04064
ACS Nano 2023, 17, 15012−15024